Radio Science, Volume 32, Number 2, Pages 657–668, March–April 1997

Impact of antenna errors on the radiometric accuracy of large aperture synthesis radiometers

A.Camps, J.Bará, F.Torres, I.Corbella, and J. Romeu

Department of Signal Theory and Communications, Universitat Politècnica de Catalunya, Barcelona, Spain

Abstract. A classification of system errors in aperture synthesis radiometry applied to Earth observation is presented. A general procedure to quantify the impact of antenna errors on the radiometric accuracy is developed and is then particularized to an L-band Y-shaped interferometer called MIRAS (microwave imaging radiometer by aperture synthesis) currently under study at the European Space Agency. This work analyzes in detail the impact of antenna errors on the radiometric accuracy of the instrument. These antenna errors are grouped into amplitude and phase antenna pattern errors, antenna position errors and antenna cross polarization errors. Special attention is paid to antenna coupling effects because of their importance in the selection of a suitable inversion algorithm for large aperture synthesis interferometers: the G-matrix techniques or the Fourier techniques proposed for MIRAS.

1. Introduction

Present climate and hydrological models lack global soil moisture and ocean salinity measured data. This information can be provided by a radiometer operating at 1.4 GHz in a Sun-synchronous dawn-dusk orbit giving 0.5-K radiometric resolution, 10-km spatial resolution, and 1-3 days revisit time [*European Space Research and Technology Centre (ESTEC),* 1995]. Classical radiometers need a steerable antenna of several tens of meters to satisfy these requirements, which is technologically unfeasible. However, aperture synthesis interferometer radiometers can cope with them by using a sparse array of small antennas and processing their outputs properly. While the performance of total power radiometers is well known and they have been used successfully, the literature about interferometer radiometers is scarce and reduces to radioastronomy [*Thompson and d'Addario,* 1982; *Thompson et al.*, 1986], the ESTAR (electronically steered thinned array radiometer) experiment [*Ruf et al.*, 1988; *LeVine et al.*, 1989; *LeVine et al.*, 1990; *Ruf,* 1991; *Tanner and Swift*, 1993] and the MIRAS (microwave imaging radiometer by aperture synthesis) prototype [*Martín-Neira et al.*, 1994; *Martín-Neira et al.*, 1996].

Paper number 96RS03198.
0048-6604/97/96RS-03198$11.00

The scenes observed in radioastronomy are very small portions of the sky, most of them consisting of point sources having spatial Fourier transforms, also called visibilities, with a nearly constant modulus. These features allow us to use highly directive antennas whose patterns can be precisely known in the field of view (FOV) and that can be spaced many wavelengths without aliasing problems in the image reconstruction process. In addition, many baselines can be generated with a single pair of antennas by using the Earth rotation synthesis, leading to systematic errors. On the other hand, from a low orbit the Earth appears as a wide thermal source filling almost completely the FOV. To cope with the wide FOV and to avoid image blurring due to satellite motion, a complete set of measurements must be obtained in a fraction of a second by a large number of small antennas whose patterns must be completely known [*Camps et al.*, 1995a; *Camps et al.*, 1995b; *Bará et al.*, 1996]. In order to preserve the required alias-free swath during the reconstruction process, these antennas must be closely spaced, increasing the coupling between them as well as the number of antennas and receivers that are needed to satisfy the spatial resolution requirements. All of these features complicate the analysis of the global performance of this instrument, as well as the calibration procedure [*Torres et al.*, 1996a] and the reconstruction algorithms [*Camps et al.*, 1995b; *Bará et al.*, 1996].

In the assessment of the performance of an interferometer radiometer, there are two kinds of errors

to be studied: errors due to concept implementation limitations and errors due to system imperfections. Concept implementation limitations are related to the properties of the physical process being measured and the conditions where the measurements are made. Discretization errors, spatial decorrelation (fringe-washing effects), and finite signal-to-noise ratio can be included in this group. The impact of these factors on the spatial resolution and the radiometric sensitivity has already been studied [*Ruf et al.*, 1988; *Bará et al.*, 1996]. System imperfections errors are related to nonidealities of system components and are classified in section 3.

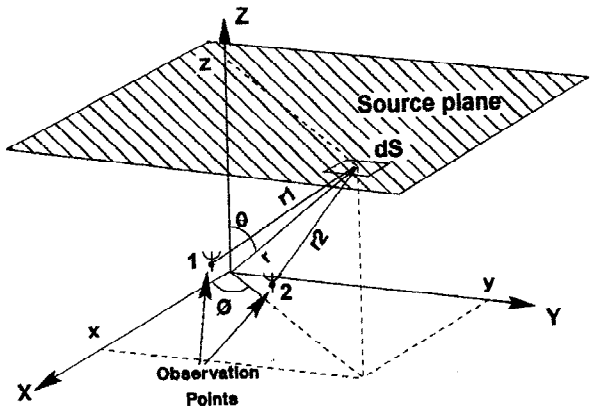

Figure 1. Antenna and thermal source geometry.

2. Basic Equations

Consider the geometry described in Figure 1. The measured spatial frequency Fourier transform, or sample of the visibility function, is given by

$$V(u,v) = \frac{1}{2Z_o} E\left[v_1(t)v_2^*(t)\right] = \iint_{\xi^2+\eta^2\le 1} T(\xi,\eta)\,\tilde{r}_{12}\left(-\frac{\Delta r}{c}\right)e^{-j2\pi(u\xi+v\eta)}d\eta\,d\xi \quad (1)$$

where (u,v) is the distance between antennas normalized to the wavelength, $v_1(t)$ and $v_2(t)$ are the analytic signals of the voltages at the output ports of antennas 1 and 2 loaded with an impedance Z_o, and $T(\xi,\eta)$ is the modified brightness temperature defined as

$$T(\xi,\eta) = \frac{T_B(\xi,\eta)}{\sqrt{1-\xi^2-\eta^2}} F_{n_1}(\xi,\eta)F_{n_2}^*(\xi,\eta) \quad (2)$$

$T_B(\xi,\eta)$ is the brightness temperature, $(\xi,\eta) = (\sin\theta \cos\phi, \sin\theta \sin\phi)$ are the director cosines with respect to the (X,Y) axes, and $\xi^2+\eta^2\le 1$, $F_n(\xi,\eta)$ is the normalized antenna voltage pattern, and the fringe-wash function is given by

$$\tilde{r}_{12}(\tau) = r_{12}(\tau)\,e^{-j\omega_o\tau}$$
$$r_{12}(\tau) = \int_{-\infty}^{+\infty} H_1(f)H_2^*(f)e^{j2\pi f\tau}df \quad (3)$$

where $H_i(f)$ is the overall frequency response normalized to unity of the ith receiver.

Note that if $v_1(t) = v_2(t)$, then $V(0,0)$ is the noise power collected by the antenna: $V(0,0) = kT_AB$. Note also that in the ideal case (no decorrelation effects $\tilde{r}_{12}(\tau)=1$ and identical antenna patterns $F_{ni}=F_{nj}=F_n$), the visibility function and the modified brightness temperature are related by a Fourier Transform:

$$T[\xi,\eta] = F^{-1}[V(u,v)] \quad (4)$$

As is apparent from (1), (2), and (3), residual antenna and receiver errors appear in the samples of the visibility function V^{raw}. However, each error is produced at a different stage in the receiving chain, allowing a classification which is very important when establishing a calibration procedure [*Torres et al.*, this issue].

3. Error Classification

Ruf [1991] studied a series of errors in the frame of the G-matrix image reconstruction method applied to the one-dimensional ESTAR experiment. The large size of the MIRAS two-dimensional array (130 antennas and 11353 visibility samples) makes unpractical the G-matrix inversion method. Consequently, antennas and receivers must have stringent tolerances to allow some kind of Fourier inversion techniques, and some kind of onboard calibration procedures must be allocated [*Torres et al.*, 1996]. Instrumental errors can be classified in two main groups: (1) antenna errors that are the subject of this paper and (2) receiver and baseline errors [*Torres et al.*, this issue]

Antenna errors affect the exploration of the scene and require known scenes to be calibrated, something unfeasible due to the lack of accurate models for natural surfaces or due to the ban on transmitting calibrating signals in protected bands [*ESTEC*, 1995]. Nevertheless, most of them can be measured on the

ground and included in an iterative inversion algorithm [*Camps et al.*, 1995b; *Bará et al.*, 1996]. Antenna imperfections are pattern and amplitude phase ripple, pattern pointing errors, position errors, vertical/horizontal cross polarization, and antenna coupling. Antenna pattern phase and gain ripples, as well as antenna pointing errors, can be grouped together into antenna voltage pattern errors, but in our study they are treated separately in order to quantify their different impacts on the radiometric resolution. The study of all the errors is performed by computing separately their impact on the radiometric accuracy. The proposed method is general and can be applied to arbitrarily shaped arrays and brightness temperature scenes. The use of the method will be demonstrated by analyzing the Y-shaped array of the MIRAS experiment and by considering a reference scene consisting of a modified brightness temperature distribution inside the Earth-sky border of 200 K and zero elsewhere

$$T(\xi,\eta)=\frac{T_B(\xi,\eta)}{\sqrt{1-\xi^2-\eta^2}}=200\ \text{K};\quad (\xi,\eta)\subset \text{Earth}(\xi,\eta) \tag{5}$$

Extended thermal sources have a low-pass spatial frequency spectrum, which means that the shorter baselines are the most significant ones. As is proved in section 4.1, the analysis results that follow are independent of the particular brightness temperature distribution and the extension of the *(u,v)* coverage, provided that it is large enough to collect a large fraction of the power, about 99.98% (equations (26) and (27)). In either case, arbitrary scenes can be analyzed by following the same procedure.

For small errors, the modified temperature distribution can be directly recovered by an inverse discrete Fourier transform

$$\begin{aligned} T^{raw}(\xi,\eta) &= F^{-1}\left[\, W(u,v)\ V^{raw}(u,v)\,\right] \\ T^{ideal}(\xi,\eta) &= F^{-1}\left[\, W(u,v)\ V^{ideal}(u,v)\,\right] \end{aligned} \tag{6}$$

where W(u,v) is a 2-D window. For larger errors, other methods should be used, i.e., the G-matrix method [*Ruf et al.*, 1988] or other iterative procedures [*Lannes and Anterrieu*, 1994; *Camps et al.*, 1995b]. In our analysis the error is estimated as the root-mean-square value of the difference between the corrupted temperature T^{raw} and the expected value:

$$\Delta T=\sqrt{\frac{1}{M-1}\sum_{l=1}^{M}\left[T^{raw}(\xi_p\eta_l)-T^{ideal}(\xi_p\eta_l)\right]^2} \tag{7}$$

where M is the number of pixels. In order to avoid aliasing effects, the error is computed in the center of the instantaneous field of view (IFOV) (Figure 2).

4. Antenna Error Analysis

Antenna errors can be classified and modeled as follows.

4.1. Antenna Pattern Errors

The correct measurement of all the visibility samples requires that all the antennas have the same radiation pattern, which is technologically unfeasible due to mechanical tolerances. These differences affect the amplitude and the phase of the antenna voltage patterns

$$F_{n_k}(\xi,\eta)=F_n(\xi,\eta)[1+\Delta F_{n_k}(\xi,\eta)]e^{j\Delta\phi_{n_k}(\xi,\eta)} \tag{8}$$

where $F_{nk}(\xi,\eta)$ is the radiation voltage pattern of antenna k, $F_n(\xi,\eta)$ is the average radiation voltage pattern of all the antennas, and $\Delta F_n(\xi,\eta)$ and $\Delta\phi_{nk}(\xi,\eta)$ are the voltage amplitude and phase errors.

The impact of antenna amplitude and phase errors over the visibility samples is derived in Appendix 1. The error in the visibility sample being measured between antennas k and l is given by

$$\Delta V_{kl}(u_{kl},v_{kl}) \approx \Delta S_{-3\,dB}\, E_{kl}(u_{kl},v_{kl})\ T_A \tag{9}$$

where

$$E_{kl}(u,v)=\iint_{\xi^2+\eta^2\le 1}\epsilon_{kl}(\xi,\eta)\ e^{j2\pi(u\xi+v\eta)}\,d\xi\,d\eta \tag{10}$$

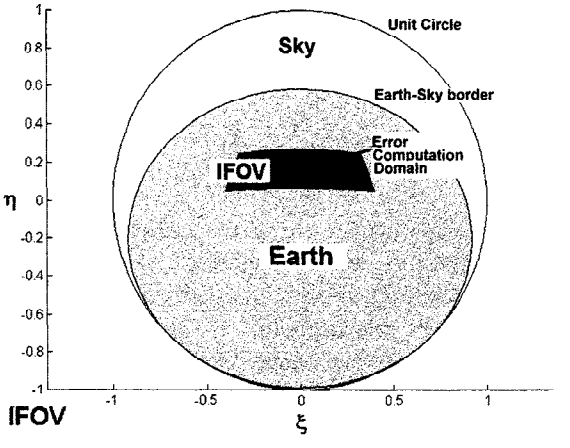

IFOV

Figure 2. Earth and sky regions in the director cosines domain from a platform of 800-km height tilted 31.2°, instantaneous FOV, and inner circle where errors are computed.

$$\epsilon_{kl}(\xi,\eta) \approx \Delta F_{n_k}(\xi,\eta) + \Delta F_{n_l}(\xi,\eta) + j(\Delta\phi_k(\xi,\eta) - \Delta\phi_l(\xi,\eta))$$

and $\Delta S_{-3\ dB}$ is the half-power bandwidth of the visibility function $V(u,v)$.

Equation (9) states that provided the visibility function has a rapid decline, the error induced in the visibility sample (u_{kl},v_{kl}) by the antenna voltage patterns is proportional to the antenna temperature and the sample (u_{kl},v_{kl}) of the Fourier transform of the antenna pattern cross error $\epsilon_{kl}(\xi,\eta)$ (equation (10)).

At this point, the temperature error and the radiometric accuracy can be computed from the visibility error by assuming that visibility errors are uncorrelated except for $V(-u,-v)$, that is, the complex conjugate of $V(u,v)$

$$\Delta T(\xi,\eta) = A\sum_m\sum_n W_{mn}\Delta V_{mn} e^{j2\pi(u_{mn}\xi + v_{mn}\eta)}$$

$$\sigma^2_{\Delta T} = <|\Delta T|^2> \approx A^2\sum_m\sum_n W^2_{mn} <|\Delta V_{mn}|^2> = A^2(\Delta S_{-3\ dB}\, T_A)^2 \sum_m\sum_n W^2_{mn} \quad (11)$$

$$E\left[\left|\iint_{\xi^2+\eta^2\le 1} \epsilon_{kl}(\xi,\eta)\, e^{j2\pi(u\xi+v\eta)} d\xi\, d\eta\right|^2\right]$$

where angle brackets denote the expectation operator and A is the (u,v) pixel area: $\sqrt{3}d^2/2$ for hexagonal sampling (Y arrays, and triangular arrays) and d^2 for rectangular sampling (T arrays). In the following sections, each antenna error is analyzed separately.

4.1.1. **Antenna pattern phase and amplitude ripple.** Typical antenna pattern errors are phase and amplitude ripples in the voltage pattern

$$\Delta\phi_k(\xi,\eta) = A_k \cos(\omega_\phi \zeta + \phi_k); \quad \zeta = \sqrt{\xi^2+\eta^2}$$
$$\Delta F_{n_k}(\xi,\eta) = A_k \cos(\omega_A \zeta + \phi_k) \quad (12)$$

which represent ripples along the radial direction in the (ξ,η) plane; A_k is the magnitude of the phase or amplitude ripple, ω_ϕ and ω_A are their frequencies, and ϕ_k is an aleatory displacement.

4.1.2. **Antenna pointing errors.** Antenna gain patterns can be fitted very well by

$$|F_n(\theta)|^2 = \cos^n(\theta) \quad (13)$$

where θ is the angle with respect to the Z axis. With pointing errors, expression (13) becomes

$$F_n(\xi,\eta) = [\xi\sin(\theta_o)\cos(\phi_o) + \eta\sin(\theta_o)\sin(\phi_o) + \sqrt{1-\xi^2-\eta^2}\cos(\theta_o)]^{\frac{n}{2}} \quad (14)$$

where (θ_o,ϕ_o) represents the direction of the antenna radiation pattern maximum.

4.2. Antenna Position Errors

The mechanical structure of a Y array consists of three arms joined at one extreme (Figure 3). The cross section of the arms is rectangular, and the resonant frequencies in the plane of the array (X,Y) and in the perpendicular direction (Z) are not necessarily equal. Accelerations/decelerations of the platform during its orbit, as well as thermal effects (dilatations/contractions), produce oscillations of the arms around their balance points. The amplitude of these vibrations is kept low enough to guarantee the correct performance of the instrument. The study can then be simplified to the first resonant mode:

$$\bar{dr}(s,t) = A_{ip_{max}}\sin\left(\frac{\pi}{2l}s\right)\sin(\alpha)\sin(\omega_{rip}t+\phi_{ip})\,\hat{x} + A_{ip_{max}}\sin\left(\frac{\pi}{2l}s\right)\cos(\alpha)\sin(\omega_{rip}t+\phi_{ip})\,\hat{y} + A_{op_{max}}\sin\left(\frac{\pi}{2l}s\right)\sin(\omega_{rop}t+\phi_{op})\,\hat{z} \quad (15)$$

where $A_{ip\ max}$ and $A_{op\ max}$ are the maximum in-plane and off-plane amplitudes of the oscillations in each arm, s is the radial distance to the joining point of the arms, α is the angle of the arm with the X axis, $\omega_{r,ip}$ and $\omega_{r,op}$ are the in-plane and off-plane resonant

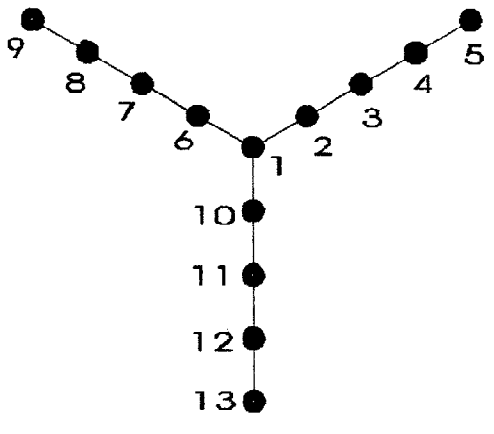

Figure 3. Geometry of a Y-shaped interferometer with three antennas per arm.

frequencies of the arm, and ϕ_{ip} and ϕ_{op} are their corresponding phases.

These oscillations induce a phase modulation in the measured voltage that produces an uncertainty in the position of the antennas and in the baseline being measured (Appendix 2)

$$\begin{aligned}\Delta u &= \Delta_x \sin\left(\frac{\omega_{rip}\tau}{2}+\theta_x\right)\mathrm{sinc}(f_{rip}\tau)\\ \Delta v &= \Delta_y \sin\left(\frac{\omega_{rip}\tau}{2}+\theta_y\right)\mathrm{sinc}(f_{rip}\tau)\\ \Delta w &= \Delta_z \sin\left(\frac{\omega_{rop}\tau}{2}+\theta_z\right)\mathrm{sinc}(f_{rop}\tau)\end{aligned} \tag{16}$$

The relationships between Δ_x, Δ_y, Δ_z, θ_x, θ_y, θ_z and the mechanical parameters $\alpha_{1,2}$, $\phi_{ip1,2}$, $\phi_{op\ 1,2}$, $A_{ip\ 1,2}$ and $A_{op\ 1,2}$ are given in equations (A11) and (A12). Baseline uncertainty can be canceled if the integration time is a multiple of the least common multiple of the in-plane and off-plane resonant periods, or it can be minimized by integrating during long periods of time, which can achieved by averaging consecutive measurements during the time the pixel remains in the FOV.

4.3. Antenna Vertical/Horizontal Cross Polarization

Antenna cross polarization between vertical and horizontal polarizations produces an error in the modified brightness temperatures given by

$$\begin{aligned}\hat{T}_H &= (1-\epsilon_{HV})T_H+\epsilon_{HV}T_V\\ \hat{T}_V &= (1-\epsilon_{HV})T_V+\epsilon_{HV}T_H\end{aligned} \tag{17}$$

The cross polarization factor ϵ_{HV} is contributed by the antenna cross polarization ratio, which is usually the dominant term, and by the error induced by the antenna pointing accuracy, which is usually negligible.

4.4. Antenna Coupling

In some interferometric radiometry fields, i.e., radioastronomy, the effect of antenna coupling is usually negligible due to the following reasons: The antennas are usually very directive and, because of the small angular extension of the scenes being imaged, the distance between the antennas is usually large. On the other hand, interferometric radiometers devoted to Earth observation require closely spaced antennas with a large half-power beam width to cope with the large FOV without aliasing problems in the image-formation process. *Ruf* [1991] stated that the interference pattern in the ESTAR unidimensional interferometric radiometer is not sinusoidal because of antenna coupling and multiple reflections in the array structure. Errors are then analyzed through the distorted interference patterns and the G-matrix inversion method. However, large two-dimensional arrays such as MIRAS would probably make use of Fourier-based inversion techniques [*Martín-Neira et al.*, 1996], and further analysis on antenna coupling errors and possible calibration methods is required.

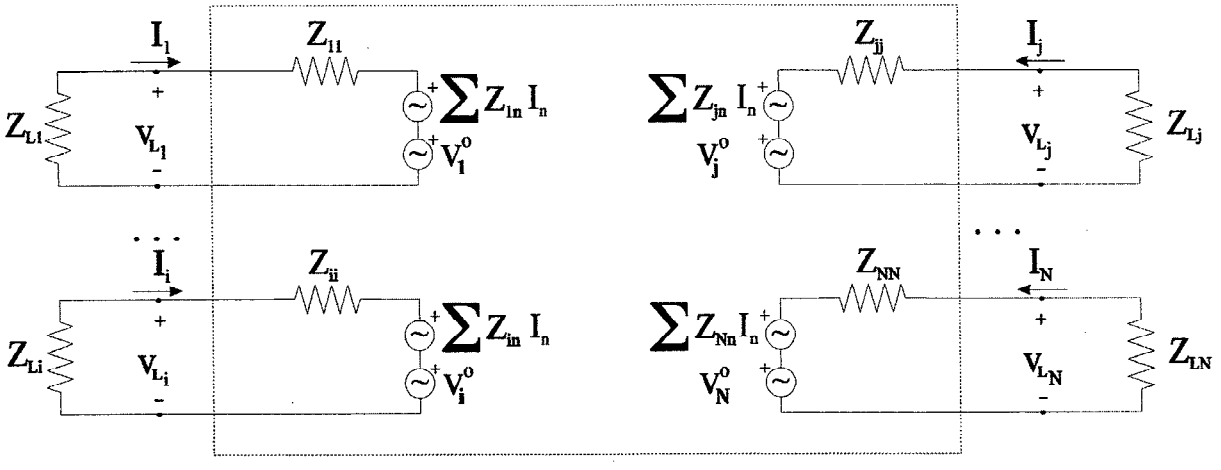

Figure 4. Interferometer antenna array as a multiport for antenna coupling analysis.

Figure 4 shows the circuit model of the antenna array. The array is treated as a multiport where each port corresponds to an antenna. The particular values of Z_{mm} *and* Z_{mn} depend on the geometry, as well as on the antenna distance and their relative orientation, and must be measured when all the antennas are mounted in the array:

$$Z_{mm} = \frac{v_m}{i_m}\Big|_{i_p=0\ \forall p\neq m} \quad ; \quad Z_{mn} = \frac{v_m}{i_n}\Big|_{i_p=0\ \forall p\neq n} \tag{18}$$

In this way, measured input and mutual impedances take into account the effect of the mechanical structure and their coupling. In equation (19) the voltage $v_{L\,m}$ is the voltage measured at the load connected to port "m" affected by load mismatches and coupling, while v^o_m is the voltage that would be measured at the "m" port when all the antennas where open-circuited, the assumption underlying the derivation of equation (1) [*Thompson et al.,* 1986]. The voltage generators account for the coupling over a particular antenna. The relationship between the loaded (subscript L) and the ideal (superscript 0) voltages can be derived from

$$\begin{bmatrix} v_{L_1} \\ v_{L_2} \\ \vdots \\ v_{L_N} \end{bmatrix} = \begin{bmatrix} Z_{11} & Z_{12} & \cdots & Z_{1N} \\ Z_{21} & Z_{22} & \cdots & Z_{2N} \\ Z_{N1} & Z_{N2} & \cdots & Z_{NN} \end{bmatrix} \begin{bmatrix} i_1 \\ i_2 \\ \vdots \\ i_N \end{bmatrix} + \begin{bmatrix} v_1^o \\ v_2^o \\ \vdots \\ v_N^o \end{bmatrix}; \tag{19}$$

$$\bar{v}_L = \bar{\bar{Z}}\,\bar{i} + \bar{v}^o$$

$$\begin{bmatrix} i_1 \\ i_2 \\ \vdots \\ i_N \end{bmatrix} = -\begin{bmatrix} v_{L_1}/Z_{L_1} \\ v_{L_2}/Z_{L_2} \\ \vdots \\ v_{L_N}/Z_{L_N} \end{bmatrix} \tag{20}$$

by substituting (20) in (19) and isolating the load voltages

$$\begin{bmatrix} v_1^o \\ v_2^o \\ \vdots \\ v_N^o \end{bmatrix} = \begin{bmatrix} 1+\frac{Z_{11}}{Z_{L_1}} & \frac{Z_{12}}{Z_{L_2}} & \cdots & \frac{Z_{1N}}{Z_{L_N}} \\ \frac{Z_{21}}{Z_{L_1}} & 1+\frac{Z_{22}}{Z_{L_2}} & \cdots & \frac{Z_{2N}}{Z_{L_N}} \\ \cdots & \cdots & \ddots & \cdots \\ \frac{Z_{N1}}{Z_{L_1}} & \frac{Z_{N2}}{Z_{L_2}} & \cdots & 1+\frac{Z_{NN}}{Z_{L_N}} \end{bmatrix} \begin{bmatrix} v_{L_1} \\ v_{L_2} \\ \vdots \\ v_{L_N} \end{bmatrix}; \tag{21}$$

$$\bar{v}^o = \bar{\bar{C}}\,\bar{v}_L$$

$$\bar{v}_L = \bar{\bar{C}}^{-1}\,\bar{v}^o$$

which states that the measured voltage is a linear combination of the open-circuit voltages. Consequently, the ideal and the measured visibilities are related by the $\bar{\bar{C}}$ matrix according to

$$\begin{aligned} \bar{\bar{V}}_L &= \frac{1}{2Z_o} E\left[\bar{v}_L\,\bar{v}_L^H\right] \\ &= \bar{\bar{C}}^{-1}\frac{1}{2Z_o} E\left[\bar{v}^o\,\bar{v}^{oH}\right]\left(\bar{\bar{C}}^{-1}\right)^H \\ &= \bar{\bar{C}}^{-1}\bar{\bar{V}}^o\left(\bar{\bar{C}}^{-1}\right)^H \end{aligned} \tag{22}$$

where the elements $V_{L\,kl}$ and V^o_{kl} of matrices $\bar{\bar{V}}_L$ and $\bar{\bar{V}}^o$ correspond to

$$\begin{aligned} V_{L_{kl}} &= \frac{1}{2Z_o} E\left[v_{L_k}\,v_{L_l}^*\right] \\ V^o_{kl} &= \frac{1}{2Z_o} E\left[v^o_k\,v^{o*}_l\right] \end{aligned} \tag{23}$$

In order to point out the significance of equation (22), let assume that we have an array formed by two equal antennas satisfying $Z_{11}=Z_{22}$, $Z_{12}=Z_{21}$, and $Z_{L1}=Z_{L2}=Z_L$. With these assumptions, the visibility sample that would be measured between antennas 1-1 and 1-2 can be computed from (22) as

$$V_{L_{11}} = \frac{1}{\left|\left(1+\frac{Z_{11}}{Z_L}\right)^2 - \frac{Z_{12}}{Z_L^2}\right|^2} \left\{-2\Re\left[\left(1+\frac{Z_{11}}{Z_L}\right)\frac{Z_{12}^*}{Z_L^*}\,V_{12}\right] + \left[\left|1+\frac{Z_{11}}{Z_L}\right|^2 + \left|\frac{Z_{12}}{Z_L}\right|^2\right]T_A\right\} \tag{24}$$

$$V_{L_{12}} = \frac{1}{\left|\left(1+\frac{Z_{11}}{Z_{L_1}}\right)^2 - \frac{Z_{12}}{Z_L^2}\right|^2} \left\{-2\Re\left[\left(1+\frac{Z_{11}}{Z_L}\right)\frac{Z_{12}^*}{Z_L^*}\right]T_A + \left|\frac{Z_{12}}{Z_L}\right|^2 V_{12}^{o\,*}\left|1+\frac{Z_{11}}{Z_L}\right|^2 V_{12}^o\right\} \tag{25}$$

where we have made use of $V^o_{11}=V^o_{22}=T_A$. Equation (24) reveals that the zero spacing visibility sample, V_{L11}, which should be constant, contains the spatial frequency V_{12}. On the other hand, equation (25) reveals that the spatial frequency sample V_{12} is

contaminated with an offset term proportional to the antenna temperature T_A. Note that the visibility sample V^o_{12} of an extended thermal source decreases at least at a $1/\rho = \lambda/r$ rate, due to the abrupt contrast between the sky and the Earth. Hence this offset term decreases with the inverse of the antenna spacing as $1/r$, because of the factor Z_{12}, and may be an important error source. These analytical results justify the shape of the interference patterns shown by *Ruf* [1991]. In a more general situation, equation (22) reveals that the measured visibilities are a linear combination of all the visibilities that can be synthesized by the array, enlarging the spatial frequency bandwidth, by transferring power from the smallest baselines to the larger ones, and by inducing high-frequency artifacts in the recovered brightness temperature distribution [*Bará et al.*, 1996]. At the same time, the decoupled visibility samples can be obtained from the coupled ones if we manage to compute or measure the $\underline{\underline{C}}$ matrix. The number of antennas in the array has an obvious influence on the coupling effect: The more antennas, the greater the coupling, but extra antennas added at the end of the Y arms have an almost negligible effect due to their smaller coupling.

This analysis is valid whenever the relative bandwidth of the signals being correlated is small enough that the measurement of the mutual impedances by means of sinusoidal signals holds, that is, the transit time between coupled antennas is small enough to consider negligible decorrelation effects, i.e., $|\tilde{r}(\tau)| \geq 0.99$.

5. Application to the MIRAS Instrument

In this section the preceding analyses are particularized for the MIRAS instrument. Since the required radiometric accuracy (1 K) and resolution (0.5 K) are very stringent [*ESTEC*, 1995], the contribution of each error source is bounded to 0.5 K, a tenth of the snapshot radiometric sensitivity predicted for MIRAS and below the expected system sensitivity after pixel averaging, 1 K [*Bará et al.*, 1996].

The study of the impact of antenna errors over the radiometric resolution requires the computation and inversion of a complete set of raw visibility samples (equations (1), (2), and (6)). According to the present MIRAS space-borne design [*Martín-Neira et al.*, 1994; *Martín-Neira et al.*, 1996], each Y arm has 43 antennas, plus a central one and three other antennas for calibration purposes. In this case, the minimum number of visibility samples to be computed is 5677, which is half the total number of nonredundant correlations, because the visibility function is Hermitian. Each visibility sample must be obtained by means of a two-dimensional numerical integration of equation (1), which poses a serious obstacle due to computing time and the available memory. However, since these errors are multiplicative, proportional to the square of the modulus of the visibility sample, simulation results for a reduced number of antennas per arm can be extrapolated to the MIRAS space-borne case, provided that the visibility function has a low-pass shape, the case of Earth observation. For the reference temperature distribution given above (equation (5)), the following numbers corroborate this assumption (visibility samples computed directly from the scene Fourier transform). (1) The MIRAS case, a Y array with 43 antennas per arm plus the central one, has 5677 visibilities.

$$\sum_n \sum_m |V(u_n,v_m)|^2 = 2.0670 \times 10^5 \qquad (26)$$

(2) In this work, a Y array with 15 antennas per arm plus the central one, 721 visibilities are computed.

$$\sum_n \sum_m |V(u_n,v_m)|^2 = 2.0666 \times 10^5 \qquad (27)$$

Computing time and memory requirements are strongly reduced down to 12.7%, while the numerical error is about 0.02%. Numerical simulations for Y arrays with 20 antennas per arm have also been performed to confirm this assumption. The fringe-wash term has been omitted since its main effect is only a small broadening of the synthesized beam in the radial direction [*Thompson and d'Addario*, 1982; *Thompson et al.*, 1986; *National Radio Astronomy Observatory (NRAO)*, 1989].

5.1. Antenna Pattern Phase and Amplitude Ripple

Experimental measurements made for three cup-dipole antennas show that $\omega_\phi \approx \omega_A = 16\pi$, while ϕ_k is a random variable. The radiometric accuracy sensibilities to antenna phase and amplitude errors are shown in Table 1 as a function of the window used: the rectangular, the triangular, the Hanning, the Hamming, and the Blackmann one with rotational symmetry and extended up to the maximum (u,v) sample being measured [*Proakis and Manolakis*, 1988]. The Blackmann window has proven its superior

Table 1. Radiometric Accuracy Sensitivity to Antenna Errors in the MIRAS case

Sensitivity $\frac{\delta T_B}{\delta \sigma_{error}}$	Rectangular	Triangular	Hamming	Hanning	Blackmann
Antenna pattern phase ripple, per degree	0.0120	0.0065	0.0092	0.0089	0.0074
Antenna pattern amplitude ripple, per percent	0.0084	0.0052	0.0065	0.0063	0.0053
Antenna pattern pointing error, per degree	0.0085	0.0054	0.0068	0.0067	0.0064
Off-plane position error, per cm	0.0046	0.0037	0.0049	0.0049	0.0046
In-plane position error, per cm	0.0019	0.0013	0.0010	0.0010	0.0010

performance in terms of robustness and noise reduction and numerical results presented make use of this window unless specified. According to the sensibility shown in Table 1, in order to achieve a 0.5-K radiometric accuracy, the maximum standard deviation of the antenna phase and amplitude errors allowed are 0.34° and 0.5%, respectively, for an average brightness temperature of 200 K. These specifications are very restrictive, but, if they cannot be met, antenna patterns can be characterized to within these specifications in order to include them in an inversion algorithm [*Camps et al.,* 1995b].

5.2. Antenna Pointing Errors

For cup-dipole antennas, pointing errors are generated by a mechanical misalignment (± 0.15°) and by an electrical phase error in the lines feeding the arms of the dipole. It has been found that equation (13) with $n = 3$ fits very well the radiation pattern of a 0.89λ-diameter cup-dipole, providing a directivity of 9 dB.

Computed radiometric accuracy sensibility to antenna pattern pointing errors is summarized in Table 1 for the windows used, as a function of the standard deviation of the angle θ_0, the angle ϕ_0 being uniformly distributed over $[0, 2\pi]$. According to the antenna pointing accuracy that can be attained, ±0.15°, the radiometric accuracy is 0.2 K for an average scene of 200 K.

5.3. Antenna Position Errors

In the initial design of the MIRAS Y arms, the in-plane and off-plane resonant frequencies are $f_{rip} = f_{rop} = 0.4$ Hz, and the integration time is limited to $\tau = 0.30$ s to avoid image blurring; the baseline errors described in equation (16) cannot be cancelled. However, they can be reduced by averaging up to 36 consecutive measurements during the time a pixel remains in the FOV: 22 s in total, 11 s at each polarization.

The computed radiometric accuracy sensibility to off-plane and in-plane position errors is given in Table 1 for different windows. Since the maximum amplitude of the oscillation is guaranteed to be 5 mm for the space-borne instrument [*European Space Agency (ESA),* 1995], the expected radiometric accuracy is $\Delta T = 0.0006\ cm^{-1}$ x0.5 cm x200 K=0.06 K for off-plane oscillations, and $\Delta T = 0.0010\ cm^{-1}$ x 0.5 cm x 200 K = 0.10 K for in-plane oscillations, and a constant 200 K test scene.

5.4. Antenna Vertical/Horizontal Cross Polarization

The cup-dipole antennas proposed for MIRAS have 25 dB of cross-polarization ratio [*ESA,* 1995] and ±0.15° pointing accuracy. The cross-polarization factor ϵ_{HV} is then dominated by the antenna cross-polarization ratio ϵ_{HV}=25 dB = 3.10^{-3} in front of the antenna accuracy $\epsilon_{HV} = \sin^2(0.15°) \approx 7.10^{-6}$.

Assuming T_{Hmax} = 300 K and T_{Vmax} = 200 K, the snapshot accuracy errors can be upper bounded by ΔT_H=0.16 K and ΔT_V=0.63 K, which are reduced by a factor of 6 after pixel averaging.

5.5. Antenna Coupling

In the MIRAS case, decorrelation effects are negligible: $\tau \leq 3$ ns, $d_{1,2} \leq 0.9$ m, B = 20 MHz, f_0 = 1.4 GHz, $0.99 \leq |\tilde{r}(\tau)| \leq 1$, and the antenna coupling theoretical analysis performed in section 4.4 holds. Mutual impedance values have been measured from three frequency-scaled 0.89λ-diameter cup-dipoles manufactured at 10.7 GHz. It is found that coupling is smaller than 30 dB for two parallel dipoles spaced 0.89λ.

In order to evaluate the impact of antenna coupling and residual calibration errors on the radiometric accuracy, two series of numerical simulations have been carried out with the experimental data. Simulation parameters are 15 antennas per arm, measured mutual and self-impedances, and Blackmann windowing. The radiometric accuracy sensibility to coupling errors has been computed for two cases: (1) antenna coupling is not calibrated at all ($\Delta T_1/T$) and (2) antenna coupling is calibrated assuming that all the parameters have their nominal values ($\Delta T_2/T$).

The first series of simulations assumes that (1) the load impedances are random Gaussian variables with $Z_L = 50\,\Omega$ mean and $\sigma_{\Delta ZL} = 2\,\Omega$ standard deviation, and (2) the parameters of the $\bar{\bar{Z}}$ matrix are random Gaussian variables whose mean corresponds to the mean measured value, and whose standard deviation is a percentage of the mean value $\sigma_{\Delta Zmn} = \alpha\, Z_{mn}$. Numerical simulations have been performed varying the parameter α in the range [0, 0.3]

$$\frac{\Delta T_1}{T} \approx 0.058; \qquad \Delta T_1 \approx 11.6K\big|_{T_0=200K}$$

$$\frac{\Delta T_2}{T} \approx 0.0034 + 0.041\,\alpha; \quad \Delta T_2 \approx 0.7K\big|_{T_0=200,\alpha=0}$$

$$\Delta T_2 \approx 1K\big|_{T_0=200,\alpha=4\,\%} \tag{28}$$

That is, even for low coupling antennas such as these cup-dipoles, $|S_{12}| \leq$ -30 dB for d=0.89λ, uncalibrated antenna coupling errors degrade significantly the radiometric accuracy. Note that the calibration exhibits a very low dependence on the variation of the input and self-impedances. On the other hand, the calibration of antenna coupling errors reduces the residual radiometric accuracy by a factor of 10, even in the case when the parameters have drifted: $\sigma_{\Delta ZL} = 2\,\Omega$ and α=4%.

The second series of simulations assumes that the load impedances have their nominal value Z_L=50Ω, and the parameters of the $\bar{\bar{Z}}$ matrix vary as above, that is, the effect of uncalibrated antenna coupling errors over the radiometric accuracy is similar.

$$\frac{\Delta T_1}{T} \approx 0.056; \qquad \Delta T_1 \approx 11.2K\big|_{T_0=200K}$$

$$\frac{\Delta T_2}{T} \approx 0.0004 + 0.069\,\alpha; \quad \Delta T_2 \approx 0.08K\big|_{T_0=200,\alpha=0}$$

$$\Delta T_2 \approx 1K\big|_{T_0=200,\alpha=7\,\%} \tag{29}$$

Again, an ideal calibration reduces the error down to the discretization threshold [*Bará et al.*, 1996]. Hence a larger incertitude in the measurement of the input and mutual impedances is allowed (7%) for a 1-K radiometric accuracy .

6. Conclusions

In this paper a general procedure to analyze the major problems associated with the antenna subsystem in a synthetic aperture interferometer radiometer has been presented. It has been found that while most of the requirements can be satisfied with the available technology (positioning and pointing accuracy, cross polarization ratios, etc.), antenna voltage patterns and coupling effects are critical and require a calibration procedure or their correction during the inversion algorithm. It has been demonstrated that mismatches between a pair of antenna voltage patterns k-l produce an error in the visibility sample $V(u_{kl}, v_{kl})$ being measured which is approximately proportional to the antenna temperature and to the (u_{kl}, v_{kl}) spectral component of the error of the product of the two antenna voltage patterns.

Theoretical analyses have been applied to analyze the impact of antenna errors over a scaled 15-antennas-per-arm Y array, with radiometric accuracy performance very close to the 43-antennas-per-arm Y array. Closely matched antenna radiation voltage patterns are required for a 0.5-K radiometric accuracy: 0.5% in amplitude and 0.34° in phase. However, if these requirements cannot be

fulfilled, antenna patterns can be measured with this precision to be included in a suitable inversion algorithm that takes into account their effects [*Camps et al.*, 1995a; *Camps et al.*, 1995b; *Martín-Neira et al.*, 1996].

Since Fourier-based inversion techniques are envisaged for large two-dimensional interferometric arrays, a technique has been proposed to quantify the impact of antenna coupling errors and calibrate them during the antenna design stage. This method, which is the main contribution of this paper, is based on the measurement of the antenna load impedances and the impedance parameters of the array over its mechanical structure with a moderate precision: 7% for 1-K radiometric accuracy. This study shows that the visibility samples being measured are a linear combination of all the visibility samples that can be synthesized by the array. These results are in concordance with the behavior of the interference patterns found in ESTAR for nonsinusoidal signals [*Ruf*, 1991].

Appendix 1. Visibility Errors due to Antenna Pattern Errors

Let $F_{nk}(\xi,\eta)$ be the normalized radiation voltage pattern of the antenna k and let $\Delta F_{nk}(\xi,\eta)$ and $\Delta\phi_k(\xi,\eta)$ be its amplitude and phase errors.

$$F_{n_k}(\xi,\eta) = F_n(\xi,\eta)\,[1+\Delta F_{n_k}(\xi,\eta)]\,e^{j\Delta\phi_k(\xi,\eta)} \quad \text{(A1)}$$

Then, the product $F_{nk}(\xi,\eta)\,F^*_{nl}(\xi,\eta)$ in (2) can be approximated by

$$\begin{aligned} &F_{n_k}(\xi,\eta)\,F_{n_l}^*(\xi,\eta) \\ &\approx |F_n(\xi,\eta)|^2\,[1+\Delta F_{n_k}(\xi,\eta) \\ &+\Delta F_{n_l}(\xi,\eta)+j(\Delta\phi_k(\xi,\eta)-\Delta\phi_l(\xi,\eta))] \\ &\triangleq |F_n(\xi,\eta)|^2\,[1+\epsilon_{kl}(\xi,\eta)] \end{aligned} \quad \text{(A2)}$$

where the term $\epsilon_{kl}(\xi,\eta)$ takes into account amplitude and phase errors and can be expanded in a Fourier series as

$$E_{kl}(u,v) = \iint_{\xi^2+\eta^2\le 1} \epsilon_{kl}(\xi',\eta')\,e^{-j2\pi(u\xi+v\eta)}d\xi\,d\eta \quad \text{(A3)}$$

The coefficient E_{kl} (p,q) is the (p,q) coefficient of the two-dimensional Fourier expansion of the antenna pattern error between antennas k and l.

At this point, assuming negligible decorrelation errors, equation (1) can be expressed as

$$\begin{aligned} V_{kl}(u,v) &= \iint_{\xi^2+\eta^2\le 1} T(\xi,\eta)[1+\epsilon_{kl}(\xi,\eta)]e^{-j2\pi(u\xi+v\eta)}d\xi\,d\eta \\ &= V^o_{kl}(u,v) + \Delta V_{kl}(\xi,\eta) \end{aligned} \quad \text{(A4)}$$

where $V_{kl}^o(u,v)$ is the ideal visibility sample measured between antennas k and l and $\Delta V_{kl}(u,v)$ is its error due to an antenna radiation pattern mismatch. Inserting (A3) in (A4), the visibility error can be expressed as

$$\begin{aligned} \Delta V_{kl} &= \\ &= \int_{-\infty-\infty}^{+\infty+\infty}\int E_{kl}(u,v) \iint_{\xi^2+\eta^2\le 1} T(\xi,\eta)e^{-j2\pi[(u_{kl}-u)\xi+(v_{kl}-v')\eta]}d\xi\,d\eta\,du'\,dv' \\ &= \int_{-\infty-\infty}^{+\infty+\infty}\int E_{kl}(u',v')\,V_{kl}(u_{kl}-u',v_{kl}-v')\,du'\,dv' \end{aligned} \quad \text{(A5)}$$

which can be approximated by

$$\Delta V_{kl} \approx \Delta S_{-3\ dB}\,E_{kl}(u_{kl},v_{kl})\,T_A \quad \text{(A6)}$$

where $\Delta S_{-3\ dB}$ is the two-dimensional half-power bandwidth in (u,v) domain. Equation (A6) holds if the visibility function is a low-pass function corresponding to an extended thermal source. Recall that the Earth is seen with an angle of vision of 120° from 800 km height.

Appendix 2. Baseline Error due to Antenna Arm Oscillation

First, the visibility function is evaluated when the distances from the source to the antennas (r_1 and r_2) are time dependent. Taking into account the basic expression given by *Thompson* [1986] and *NRAO* [1989],

$$V_{12} = \frac{1}{2Z_o}\,E\left[v_1\left(t-\frac{r_1}{c}\right)v_2^*\left(t-\frac{r_2}{c}\right)\right] \quad \text{(A7)}$$

which is also valid when $r_1 = r_1(t)$ and $r_2 = r_2(t)$. If the time dependence of $r_1(t)$ and $r_2(t)$ is assumed to be sinusoidal in the in-plane (subscript *ip*) and in the off-plane (subscript *op*) directions

$$\begin{aligned} \bar{r}_i(t) &= (x_{o_i} - A_{ip_i}\sin(\alpha_i)\sin(\omega_{rip}t+\phi_{ip_i}))\,\hat{x} \\ &+(y_{o_i}+A_{ip_i}\cos(\alpha_i)\sin(\omega_{rip}t+\phi_{ip_i}))\,\hat{y} \\ &+(z_{o_i}+A_{op_i}\sin(\omega_{rop}t+\phi_{op_i}))\,\hat{z} \qquad i = 1,2 \end{aligned} \quad \text{(A8)}$$

If $\Delta r(t) \approx \Delta r_o + \Delta r'(t)$, (A7) can be rewritten as

$$V_{12} = \frac{1}{2r_1 r_2} R_A\left(\frac{\Delta r_o}{c}\right) E\left[e^{jk_o \Delta r'(t)}\right] \quad \text{(A9)}$$

assuming that $R_A(t)$ is a smooth function, $\Delta r'(t) << \Delta r_o$, and $\Delta r'(t)/c << 1/B$

$$\begin{aligned}\Delta r(t) = |\overline{r_2} - \overline{r_1}| \approx -\left[(x_{o_2} - x_{o_1})\xi + (y_{o_2} - y_{o_1})\eta + (z_{o_2} - z_{o_1})\gamma\right] \\ -[(-A_{ip_2}\sin\alpha_2 \sin(w_{rip}t + \phi_{ip_2} + \pi) + A_{ip_1}\sin\alpha_1 \sin(w_{rip}t + \phi_{ip_1}))\xi \\ +(A_{ip_2}\cos\alpha_2 \sin(w_{rip}t + \phi_{ip_2}) - A_{ip_1}\cos\alpha_1 \sin(w_{rip}t + \phi_{ip_1} + \pi)) \\ +(A_{op_2}\sin(w_{rop}t + \phi_{op_2}) + A_{op_1}\sin(w_{rop}t + \phi_{op_1} + \pi))\gamma]\end{aligned} \quad \text{(A10)}$$

Defining

$$\begin{aligned}\lambda^2\Delta_x^2 &= A_{ip_1}^2\sin^2\alpha_1 + A_{ip_2}^2\sin^2\alpha_2 \\ &\quad -2A_{ip_1}A_{ip_2}\sin\alpha_1\sin\alpha_2\cos(\phi_{ip_1} - \phi_{ip_2}) \\ \lambda^2\Delta_y^2 &= A_{ip_1}^2\cos^2\alpha_1 + A_{ip_2}^2\cos^2\alpha_2 \\ &\quad -2A_{ip_1}A_{ip_2}\cos\alpha_1\cos\alpha_2\cos(\phi_{ip_1} - \phi_{ip_2}) \\ \lambda^2\Delta_z^2 &= A_{op_1}^2 + A_{op_2}^2 - 2A_{op_1}A_{op_2}\cos(\phi_{op_1} - \phi_{op_2})\end{aligned} \quad \text{(A11)}$$

$$\begin{aligned}tg\theta_x &= \frac{A_{ip_1}\sin\alpha_1\sin\phi_{ip_1} - A_{ip_2}\sin\alpha_2\sin\phi_{ip_2}}{A_{ip_1}\sin\alpha_1\cos\phi_{ip_1} - A_{ip_2}\sin\alpha_2\cos\phi_{ip_2}} \\ tg\theta_y &= \frac{-A_{ip_1}\cos\alpha_1\sin\phi_{ip_1} + A_{ip_2}\cos\alpha_2\sin\phi_{ip_2}}{-A_{ip_1}\cos\alpha_1\cos\phi_{ip_1} + A_{ip_2}\cos\alpha_2\cos\phi_{ip_2}} \\ tg\theta_z &= \frac{-A_{op_1}\sin\phi_{op_1} + A_{op_2}\sin\phi_{op_2}}{-A_{op_1}\cos\phi_{op_1} + A_{op_2}\cos\phi_{op_2}}\end{aligned} \quad \text{(A12)}$$

leads to

$$\begin{aligned}\Delta r(t) &= \Delta r_o(t) + \Delta r'(t) \\ &= -u\xi + v\eta + w\gamma)\lambda - [\Delta_x \sin(w_{rip}t + \theta_x)\xi \\ &\quad + \Delta_y \sin(w_{rip}t + \theta_y)\eta + \Delta_z \sin(w_{rop}t + \theta_z)\gamma]\lambda\end{aligned} \quad \text{(A13)}$$

which induces a frequency modulation

$$E_\tau\left[e^{jk_o\Delta r(t)}\right] = E_\tau\left[e^{j2\pi\frac{\Delta r(t)}{\lambda}}\right]$$

$$\begin{aligned}&= e^{-j2\pi(u\xi + v\eta + w\gamma)} \\ &E_\tau\left[e^{-j2\pi(\Delta_x \sin(w_{rip}t + \theta_x)\xi + \Delta_y \sin(w_{rip}t + \theta_y)\eta + \Delta_z \sin(w_{rop}t + \theta_z)\gamma)}\right]\end{aligned} \quad \text{(A14)}$$

where E_τ stands for the expectation operator over a finite integration time τ. If the displacements are small, $2\pi\Delta_X$, $2\pi\Delta_Y$, $2\pi\Delta_Z << 1$, the expression for the baseline error reduces to

$$\begin{aligned}E_\tau[e^{jk_o\Delta r(t)}] &= e^{-j2\pi(u\xi + v\eta + w\gamma)}[1 \\ &\quad - j2\pi\Delta_x\xi\sin\left(\frac{w_{rip}\tau}{2} + \theta_x\right)\mathrm{sinc}(f_{rip}\tau) \\ &\quad - j2\pi\Delta_y\eta\sin\left(\frac{w_{rip}\tau}{2} + \theta_y\right)\mathrm{sinc}(f_{rip}\tau) \\ &\quad - j2\pi\Delta_z\gamma\sin\left(\frac{w_{rop}\tau}{2} + \theta_z\right)\mathrm{sinc}(f_{rop}\tau)] \\ &\approx e^{-j2\pi[(u+\Delta u)\xi + (v+\Delta v)\eta + (w+\Delta w)\gamma]}\end{aligned} \quad \text{(A15)}$$

where

$$\begin{aligned}\Delta u &= \Delta_x\sin\left(\frac{\omega_{r_{ip}}\tau}{2} + \theta_x\right)\mathrm{sinc}(f_{r_{ip}}\tau) \\ \Delta v &= \Delta_y\sin\left(\frac{\omega_{r_{ip}}\tau}{2} + \theta_y\right)\mathrm{sinc}(f_{r_{ip}}\tau) \\ \Delta w &= \Delta_z\sin\left(\frac{\omega_{r_{op}}\tau}{2} + \theta_z\right)\mathrm{sinc}(f_{r_{op}}\tau)\end{aligned} \quad \text{(A16)}$$

Acknowledgments. This work has been supported by the European Space Agency within the MIRAS Rider 2 activities, Matra Marconi Space being the main contractor. We would like to thank Martín-Neira, of ESA, for his helpful discussions throughout this work.

References

Bará, J., A. Camps, I. Corbella, and F. Torres, Bi-dimensional discrete formulation for aperture synthesis radiometers, *contract 9777/92/NL/PB,* final report, Eur. Space Agency-Eur. Space Res. and Technol. Cent., Noordwijk, Netherlands, 1996.

Camps, A., J. Bará, I. Corbella, and F. Torres, Visibility inversion algorithms over hexagonal sampling grids, in *Proceedings of the Soil Moisture and Ocean Salinity Measurements and Radiometer Techniques Consultative*

Meeting, pp. 109-114, Eur. Space Agency-Eur. Space Res. and Technol. Cent., Noordwijk, Netherlands, 1995a.

Camps, A., J. Bará, I. Corbella, and F. Torres, Inversion algorithms over hexagonal grids in interferometric aperture synthesis radiometers, paper presented at the Progress in Electromagnetics Research Symposium, Univ. of Wash., Seattle, 1995b.

European Space Research and Technology Centre, Conclusions and recommendations from the SMOS and Summary Reports of the Working Groups, SMOS: Consultative Meeting on Soil Moisture and Ocean Salinity: Measurements and Radiometer Techniques, *ESA WPP-87,* pp. 6-11, Eur. space Res. and Technol. Cent., Noordwijk, Netherlands, 1995.

European Space Agency, MIRAS: Microwave imaging radiometer with aperture synthesis: Microwave radiometry critical technical development, final report, contract 9777/92/NL/PB, Eur. Space Agency-Eur. Space Res. and Technol. Cent., Noordwijk, Netherlands, 1995.

Lannes, A., and E. Anterrieu, Image reconstruction methods for remote sensing by aperture synthesis, paper presented at the International Geoscience and Remote Sensing Symposium, Calif. Inst. of Technol., Pasadena, Aug. 8-12, 1994.

LeVine, D.M., T.T. Wilheit, R.E. Murphy, and C.T. Swift, A multifrequency microwave radiometer of the future, IEEE Trans. Geosci. Remote Sens., *27*(2), 193-199, 1989.

LeVine, D.M., M. Kao, A.B. Tanner, C.T. Swift, and A. Griffs, Initial results in the development of a synthetic aperture microwave radiometer, IEEE Trans. Geosci. Remote Sens., *28*(4), 614-619, 1990.

Martín-Neira, M., Y. Menard, J.M. Goutoule, and U. Kraft, MIRAS, a two-dimensional aperture synthesis radiometer, paper presented at the International Geoscience and Remote Sensing Symposium, Calif. Inst. of Technol., Pasadena, Aug. 8-12, 1994.

Martín-Neira, M., et al., Integration of MIRAS breadboard and future activities, paper presented at the International Geoscience and Remote Sensing Symposium, Lincoln, Nebr., May 1996.

National Radio Astronomy Observatory, *A Collection of Lectures From the Third NRAO Synthesis Imaging Summer School,* vol. 6, pp. 247-258, Astron. Soc. of the Pacific, San Francisco, Calif., 1989.

Proakis, J.G., and D.G. Manolakis, *Introduction to Digital Signal Processing,* Macmillan, New York, 1988.

Ruf, C.S., Error analysis of image reconstruction by a synthetic aperture interferometric radiometer, *Radio Sci., 26*(6), 1419-1434, 1991.

Ruf, C.S., C.T. Swift, A.B. Tanner, and D.M. LeVine, Interferometric synthetic aperture radiometry for the remote sensing of the Earth, *IEEE Trans. Geosci. Remote Sens., 26*(5), 597-611, 1988.

Tanner, A.B., and C.T. Swift, Calibration of a synthetic aperture radiometer, *IEEE Trans. Geosci. Remote Sens., 31*(1), 257-267, 1995.

Thompson, A.R., and L.R. d'Addario, Frequency response of a synthesis array: Performance limitations and design tolerances, *Radio Sci., 17*(2), 357-369, 1982.

Thompson, A.R., J.M. Moran, and G.W. Swenson, *Interferometry and Synthesis in Radio Astronomy,* 169-174, 184-206, John Wiley, 1986.

Torres, F., A. Camps, J. Bará, I. Corbella, R. Ferrero, Onboard phase and module calibration of large aperture synthesis radiometers. Study applied to MIRAS, *IEEE Trans. Geosci. Remote Sens., 34*(4), 1000-1009, 1996.

Torres, F., A. Camps, J. Bará, and I. Corbella, Impact of receiver errors on the radiometric resolution of large two-dimensional aperture synthesis radiometers, *Radio Sci.,* this issue.

J. Bará, A. Camps, I. Corbella, F. Torres, and J. Romeu, Department of Signal Theory and Communications, Universitat Politècnica de Catalunya, 08034 Barcelona, Spain. (e-mail: tscjbt@eupbl.upc.es; camps@voltor.upc.es; corbella@voltor.upc.es; torres@voltor.upc.es; romeu@voltor.upc.es)

(Received June 14, 1996; revised October 9, 1996; accepted October 21, 1996.)